Two Leading ENSO Modes and El Niño Types in the Zebiak–Cane Model

RUIHUANG XIE

Key Laboratory of Ocean Circulation and Waves, Institute of Oceanology, Chinese Academy of Sciences, and Laboratory for Ocean and Climate Dynamics, Qingdao National Laboratory for Marine Science and Technology, Qingdao, China

FEI-FEI JIN

Department of Atmospheric Sciences, School of Ocean and Earth Science and Technology, University of Hawai'i at Mānoa, Honolulu, Hawaii

(Manuscript received 13 July 2017, in final form 12 December 2017)

ABSTRACT

Modern instrumental records reveal that El Niño events differ in their spatial patterns and temporal evolutions. Attempts have been made to categorize them roughly into two main types: eastern Pacific (EP; or cold tongue) and central Pacific (CP; or warm pool) El Niño events. In this study, a modified version of the Zebiak–Cane (MZC) coupled model is used to examine the dynamics of these two types of El Niño events. Linear eigenanalysis of the model is conducted to show that there are two leading El Niño–Southern Oscillation (ENSO) modes with their SST patterns resembling those of two types of El Niño. Thus, they are referred to as the EP and CP ENSO modes. These two modes are sensitive to changes in the mean states. The heat budget analyses demonstrate that the EP (CP) mode is dominated by thermocline (zonal advective) feedback. Therefore, the weak (strong) mean wind stress and deep (shallow) mean thermocline prefer the EP (CP) ENSO mode because of the relative dominance of thermocline (zonal advective) feedback under such a mean state. Consistent with the linear stability analysis, the occurrence ratio of CP/EP El Niño events in the nonlinear simulations generally increases toward the regime where the linear CP ENSO mode has relatively higher growth rate. These analyses suggest that the coexistence of two leading ENSO modes is responsible for two types of El Niño simulated in the MZC model. This model result may provide a plausible scenario for the observed ENSO diversity.

1. Introduction

El Niño–Southern Oscillation (ENSO) is the source of the most energetic sea surface temperature (SST) variation in the tropical Pacific on the interannual time scale. El Niño and La Niña events vary from event to event in their characteristics. In addition to the conventional eastern Pacific (EP) El Niño events with the strongest SST anomalies (SSTAs) in the eastern Pacific (such as the 1982/83 and 1997/98 events), a different type of El Niño that has its maximum SSTA more in the central Pacific has become a common occurrence since the late 1990s. These two types of El Niño events have received increasing attention (Capotondi et al. 2015).

Various terminology, such as date line El Niño (Larkin and Harrison 2005), El Niño Modoki (Ashok et al. 2007), central Pacific (CP) El Niño (Kao and Yu 2009), and warm pool El Niño (Kug et al. 2009), have been utilized to describe the second type of El Niño events, which includes the typical 2002/03, 2004/05, and 2009/10 events. This CP El Niño has been regarded as a dynamically distinct type from the EP El Niño (Kug et al. 2009; Karnauskas 2013). However, this distinction has been disputed by Giese and Ray (2011) who showed that the locations of El Niño SSTA maxima through the twentieth century were normally distributed with most locations in the central Pacific. They suggested that the EP and CP El Niño events were simply a part of a continuum of patterns. However, the limited length of data makes it difficult to draw conclusions based on the statistics.

Despite the diverse ENSO behaviors, dividing ENSO approximately into two basic types is the first step to understand the ENSO diversity/complexity. It has been

Denotes content that is immediately available upon publication as open access.

Corresponding author: Dr. Fei-Fei Jin, jff@hawaii.edu

DOI: 10.1175/JCLI-D-17-0469.1

© 2018 American Meteorological Society. For information regarding reuse of this content and general copyright information, consult the AMS Copyright Policy (www.ametsoc.org/PUBSReuseLicenses).

noted that dominant mechanisms differ for the two types of El Niño events (e.g., Kug et al. 2009, 2010; Karnauskas 2013). One may examine the main contributing terms of ENSO positive feedback processes to delineate the differences in the dynamics of the two-type events. Following Jin et al. (2006), the main contributing terms for SST growth in the SST equation [e.g., Eq. (A7) in the appendix] can be abbreviated as follows:

$$\frac{\partial T'}{\partial t} \sim -u_1' \frac{\partial \overline{T}}{\partial x} + \overline{w_s} \frac{T'_{\rm sub}}{H_1} - w_s' \frac{\partial \overline{T}}{\partial z}. \qquad (1)$$

Here, the variable with an overbar represents the mean state, and the variable with a prime denotes the anomaly that departs from the mean state. The right-hand-side terms are the three positive feedbacks that contribute to the SSTA growth (Jin et al. 2006; Ren and Jin 2013): the zonal advective feedback (ZA, *advection of mean temperature by anomalous zonal currents* u_1'), the thermocline feedback (TH, *vertical advection of anomalous subsurface temperature* $T'_{\rm sub}$ by mean upwelling $\overline{w_s}$), and the Ekman feedback (EK, *vertical advection of mean ocean temperature by anomalous upwelling* w_s').

Kug et al. (2009) concluded that the observed EP El Niño events are dominated by TH feedback, whereas ZA plays a more important role in CP El Niño events, and EK plays a minor role in both types of El Niño. This distinction between EP and CP events was confirmed by diagnostic results from some climate models that can reproduce the two types of El Niño (Kug et al. 2010; Capotondi 2013). In particular, Kug et al. (2009, 2010) showed that the oceanic heat content recharge/discharge processes, which influence SSTA through TH, is evident in the EP El Niño events, whereas it is nearly absent in the CP El Niño events. However, some recent studies (Ren and Jin, 2013; Xie et al. 2015a) have indicated that the recharge/discharge processes exist in both types of El Niño, and they further argued that TH and ZA contribute jointly to the development of both types of El Niño events, whereas ZA provides the main negative contribution to the phase transitions. Therefore, the two types of El Niño (ENSO) events can be conceptualized in the same recharge/discharge oscillator theory with the inclusion of ZA in its contribution to the phase transitions of both El Niño types (Ren and Jin 2013).

Previous studies (Kao and Yu 2009; Furtado et al. 2012; Ren et al. 2013) have shown that EP ENSO is characterized by a significant peak in the 3–5-yr band, whereas the CP ENSO shows a major peak around two years. Ren et al. (2013) suggested that the observed EP and CP ENSO events were closely related to the quasi-quadrennial (QQ) and quasi-biennial (QB) ENSO modes that were obtained theoretically by Bejarano (2006) and Bejarano and Jin (2008, hereafter BJ08) in a version of the Zebiak–Cane (ZC) model (Zebiak and Cane 1987, hereafter ZC87). According to BJ08, the QQ ENSO mode is dynamically controlled by TH and has its SSTA center in the eastern Pacific, while the QB ENSO mode is dominated by ZA and shows a SSTA center located farther westward than the QQ mode. In addition, two similar ENSO-like modes, a low-frequency remote mode in the eastern Pacific that is triggered by the wind stress in the western-central Pacific and a fast local SST mode in the central Pacific which is controlled by local winds and ocean currents, were noted in Fedorov and Philander (2000) and Fedorov and Philander (2001, hereafter FP01), whose findings can be further traced back to some earlier theoretical ENSO studies (Jin and Neelin 1993a,b; Jin 1997a,b; An and Jin 2000, 2001).

This study extends the framework of BJ08 in a new version of ZC-type model, which includes a modified atmospheric component for improving the surface wind response to SSTA, and updated mean states to re-examine the characteristics of the two leading ENSO modes and their relevance to the observed and simulated two types of El Niño event. We attempt to explore the instability, periodicity, and patterns of the two leading ENSO modes in a broad range of mean climate conditions. This paper is organized as follows. Section 2 introduces the improved atmospheric model and the updated mean states. Section 3 presents the dependence of the diverse ENSO modes in a linearized ZC-type model on the mean states and discusses the underlying mechanisms. Section 4 shows the consistency between the linear stability of two leading ENSO modes and simulated El Niño types in the nonlinear ZC model. Section 5 summarizes the main findings.

2. Model

a. Improved model

We adopt the intermediate complexity coupled model of ZC87 that has been used for over three decades to understand and predict ENSO. It is an anomaly model that consists of simple atmospheric and oceanic components. The atmospheric component is a Gill-type (Gill 1980) linear atmospheric model describing the atmospheric response to ENSO SST anomalies, and the oceanic component comprises a 1.5-layer reduced-gravity model that is forced by wind stress from the atmospheric model. Together with an embedded mixed layer SST model with a constant depth (50 m), the oceanic model can reproduce the dynamics and thermodynamics of the SST anomalies. The atmosphere and

ocean are coupled in a simple way: the atmosphere model generates anomalous wind stress through a parameterized atmospheric heating anomaly that is computed from the SST and convergence anomalies, and then the ocean model is driven by such wind stress anomalies to yield anomalous ocean currents and thermocline fluctuations to alter SST anomalies. The active domain of the model includes the tropical Pacific only (29°S–29°N, 124°E–80°W).

Our version of ZC model differs from that of BJ08 and ZC87 mainly in its atmospheric component. We modified the original model to suppress the spurious wind response in the eastern Pacific (Xie et al. 2015b; see also the appendix). We introduced a heating efficiency factor that depends on the SST and wind convergence states. This factor has a value of 100% under conditions of high SST (>27.5°C) and convergent wind, it decreases as SST decreases or wind becomes divergent. With this modification, the heating anomalies over the western and central Pacific are nearly unchanged, while those over the eastern Pacific are reduced, suppressing the spurious wind responses. Furthermore, we reduced the atmospheric convergence feedback to reduce the heating anomalies but added the effect of the convective momentum transport (CMT) into the zonal momentum equation. In some previous studies, CMT has been used to improve the wind anomalies and ENSO simulations in several complex climate models (Wu et al. 2007; Kim et al. 2008; Neale et al. 2008; Guilyardi et al. 2009). In the modified ZC model, CMT was parameterized as the vertical transport of the climatological vertical wind shear carried by anomalous convergence. The inclusion of CMT enhanced the low-level westerly wind response to El Niño. We found that CMT is more effective in the central Pacific than in the eastern Pacific because of the stronger convergence/convection anomalies in the central Pacific. As a result, the new atmospheric model improves the simulations of wind anomalies in both the central and eastern Pacific (Xie et al. 2015b).

The oceanic component model is similar to the one used in BJ08. By their modifications, it differs from the original version in the following ways. First, the oceanic wave dynamics were expressed in terms of the Hermite functions following Battisti (1988) and the details were well documented in Bejarano (2006). Second, the zonal resolution of the oceanic wave dynamics was reduced to 5.2°. These two modifications help to reduce the degrees of freedom in the model. Third, the linear damping in the oceanic momentum and continuity equations was set to zero. Last, the Heaviside function in the original model was replaced by a hyperbolic tangent function for a smoother change around zero [Eq. (A9) in the appendix]. Interested readers are referred to Bejarano (2006), BJ08, and Xie et al. (2015b) for the details of the modifications in the atmospheric and oceanic models.

b. *Updated mean states*

In ZC87, the ocean dynamics model was spun up using the mean wind stress to generate the oceanic mean states, which include horizontal surface currents, upwelling velocity at the bottom of the mixing layer, and the equatorial thermocline depth. Here, the new standard mean state is constructed in the same approach but forced by the climatological monthly mean wind stress during the period of 1980–2000. The reference wind stress is calculated from NCEP–DOE Reanalysis II (Kanamitsu et al. 2002), and the reference SST is from NOAA OISST (Reynolds et al. 2002). The standard oceanic upper-layer depth is set to 150 m. Following the approach of BJ08, additional mean states are generated by perturbing the mean wind stress S and the upper-layer depth H to spin up the oceanic model. Here H is changed from 130 to 160 m with an increment of 1 m, and S is varied from 80% to 120% of the observed intensity with an increment of 1%. It is thus just a varying factor multiplied on to the observed wind stress at each grid. It should be noted that H is a constant part of oceanic upper-layer depth, a parameter for uniformly deeper or shallower upper layer as it increases or decreases. The spatially varying part of the thermocline depth in the mean state changes consistently with the mean wind stress, so does for the mean state temperature. Generally, a small H and a strong mean wind stress correspond to a basic state with shallow thermocline and strong cold tongue, or a mean state showing La Niña–like change from the observed one. This kind of mean-state regime is in the top-left domain of Fig. 1. To the other end, a large H and a weak mean wind stress correspond to a deep thermocline and weak cold tongue, or a mean state with El Niña–like change from the observation. This kind of mean state regime is in the lower-right domain of Fig. 1. The standard mean state, including its mean wind stress, SST, ocean currents, and equatorial thermocline depth is shown in the appendix (see Fig. A1).

Finally, an array of 1270 new mean states are constructed around the new standard mean state (named H150S100), and some basic features are shown in Fig. 1 in a two-dimensional H–S space. Taking the equatorial eastern Pacific (5°S–5°N, 160°–90°W) and western Pacific (5°S–5°N, 120°E–180°) as examples, the entire mean states change slowly and continuously when H and S are varied. When the upper-layer thickness is reduced and the mean wind stress is strengthened (toward the top-left corner of the H–S space), the eastern Pacific SST is lower (Fig. 1a) and the thermocline is shallower (Fig. 1c),

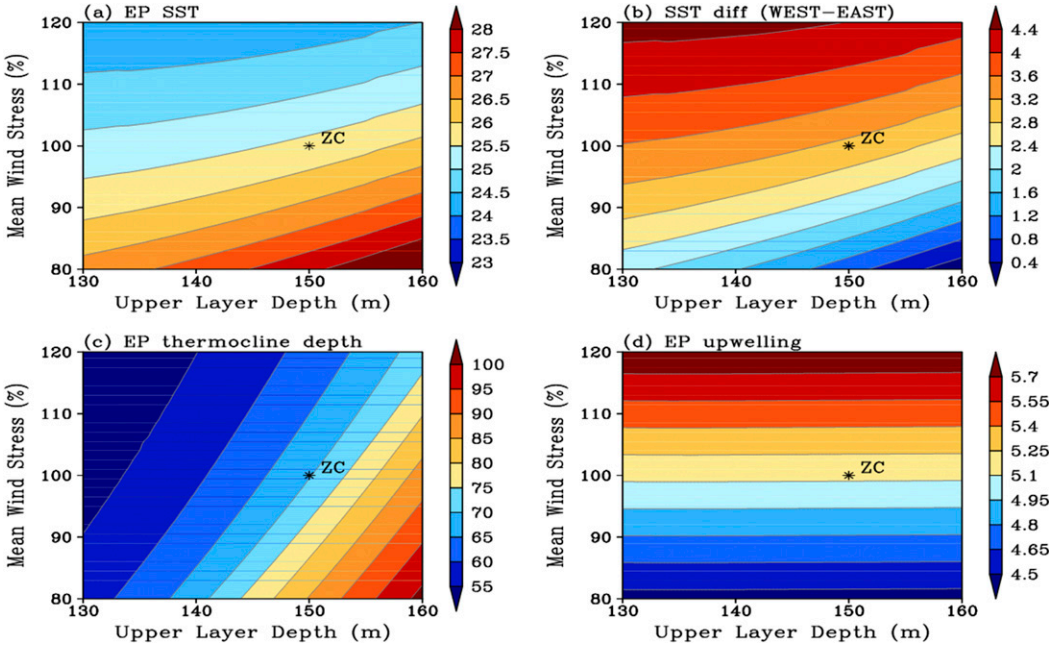

FIG. 1. The entire mean states from the oceanic component of the Zebiak–Cane model when perturbing the upper-layer depth and/or the mean wind stress. (a) Mean SST (°C) averaged over the eastern Pacific (EP, 5°S–5°N, 160°–90°W). (b) Mean zonal SST difference (°C) between the western Pacific (WP, 5°S–5°N, 120°W–180°) and EP. (c),(d) As in (a), but for the mean thermocline depth (m) and vertical velocity (10^{-6} m s^{-1}), respectively. The four variables are shown as functions of the percentages of the observational mean wind stress (%) and the oceanic upper-layer depth (m).

meanwhile the cross-basin SST difference is larger (Fig. 1b). Toward the lower-right corner of the H–S space, the mean state changes conversely. The upwelling velocity varies proportionally to the mean wind stress (Fig. 1d). In fact, these mean states are very similar to those in BJ08.

3. Two leading linear ENSO modes and their dynamics

Our modified ZC model (hereafter MZC) is then linearized following the linearization approach of BJ08. The final linear system of the MZC model can be written as

$$\frac{d\mathbf{X}(t)}{dt} = \mathbf{L}[\overline{\mathbf{X}}(H,S),\mathbf{P}]\mathbf{X}(t), \qquad (2)$$

where $\mathbf{X}(t)$ represents the state vectors that include the ocean waves and SSTA components. The wind stress anomalies can be obtained from the SSTA component in the linearized atmospheric model, and the ocean currents and thermocline depth anomalies can be calculated from ocean wave components in the ocean dynamics model. As in BJ08, this state vector has a dimension of 1439 (899 for ocean wave components and 540 for SSTA components) under the current model resolution. The Jacobian matrix $\mathbf{L}[\overline{\mathbf{X}}(H, S), \mathbf{P}]$ is obtained by linearizing the model equations with respect to each mean state $\overline{\mathbf{X}}(H, S)$ and parameter vector $\mathbf{P}$ that contains a number of model parameters, such as the thermal damping rate of SST, the entrainment efficiency, the atmospheric feedback efficiency, and etc. After the linearization, a linear stability analysis is performed to obtain the eigensolutions. The eigenvalues contain the growth rates and periods of the modes, and the corresponding eigenvectors carry the spatial structures. The numbers of the eigensolutions are equal to the degrees of freedom of the matrix $\mathbf{L}$, and each solution is independent from the other. All the modes are sorted according to their growth rates. The modes have positive (negative) growth rate means that they are unstable (stable). The most unstable or least damped modes are always on the top. All modes change continuously following the changes in the model mean state and/or parameters. Using such continuity, we can trace the leading modes along with any changes in the mean state. In our study and also early studies of Jin (1997b) and BJ08 for instance, there are two and only two leading modes standing out, whereas the rest are all strongly damped. The two leading modes, both of ENSO likeness, are near critical or unstable for most of the

mean states and reasonable parameter ranges. We excluded the annual cycle in the basic state, although the linear stability analysis with the annual cycle in the mean state can be performed by Floquet exponent analysis following the approach of Jin et al. (1996). Another reason for the exclusion of the annual cycle is because the dynamics of the most unstable ENSO mode(s) of the ZC model with a seasonally varying mean state are similar as those with the annual mean state (Jin et al. 1996; Thompson and Battisti 2000).

a. Dependence of two leading ENSO modes on mean states

As it has been demonstrated by BJ08, the ENSO modes of the linearized ZC model are sensitive to the number of key parameters. One of them is the entrainment efficiency γ [see Eq. (A8) in the appendix]. It represents the efficiency of the subsurface temperature anomalies in affecting the temperature anomalies in the mixed layer and thus directly controls the strength of the thermocline feedback (TH). In BJ08, when the efficiency factor is set at $\gamma = 0.75$ as in the original ZC model, the two leading ENSO modes of the linearized ZC model have codimension 2 degeneracy (see Fig. 4 in BJ08) under a certain basic state not far from the observed mean state. At this degeneracy, the two complex eigenvalues become identical though their eigenvectors still differ. Near this degeneracy, the two leading modes are very sensitive to small changes to the mean basic state. This degeneracy also occurs in our analysis using the new version of model and new mean states (figure not shown). However, it disappears when we adopt a moderate entrainment efficiency ($\gamma = 0.5$). As $\gamma = 0.5$ is perhaps a more suitable value for this parameter (Thompson and Battisti 2000), we will focus on this regime in which the two leading modes do not degenerate. The sensitivity of this degeneracy in the parameter space and its significance for the coexistence of two leading modes is beyond the scope of this paper and will be discussed elsewhere.

For any given set of mean state and parameter, the linear model has 1439 eigenmodes. There are two distinct, least damped or unstable, and oscillatory modes that are outstanding from the rest of all eigenmodes of the system. The slow-paced mode (mode I) has its period of mostly more than 3 years (Fig. 2a) and the other one (mode II) has a period between 1.5 and 3 years (Fig. 2c). Generally, the periods of the two modes decrease as S and/or H increases (Figs. 2a,c), which is consistent with BJ08 and with Manucharyan and Fedorov (2014) as well, although they used a more complex climate model. In particular, mode II displays a more clear dependence of its period on the mean states, that is, the period increases linearly with the decrease of S and/or H (Fig. 2c). The growth rate of mode I increases when S and H increase (toward the top-right corner of the H–S space, Fig. 2b). Unlike mode I, the growth rate of mode II increases rapidly toward the top-left corner of the H–S space (Fig. 2d). Overall, the growth rates and periods of the two leading modes and their dependence on the mean states revealed in the new version of ZC model are similar to those of BJ08.

The growth rate diagrams indicate that the two leading modes are both unstable for nearly half of the entire mean states (Figs. 2b,d). At the new standard mean state H150S100 that represents the climate condition during 1980–2000, mode I is unstable while mode II is damped. Mode I has a growth rate of $\sim 0.25\,\mathrm{yr}^{-1}$ (star in Fig. 2b), which is similar to those obtained using a similar mean state [e.g., $0.33\,\mathrm{yr}^{-1}$ in Kang et al. (2004); $0.36\,\mathrm{yr}^{-1}$ in Xie et al. (2015a)]. The super criticality of mode I and subcriticality of mode II implies the dominance of mode I, and it is consistent with the observed ENSO variability during 1980–2000 when the quasi-quadrennial variability was more active (Kao and Yu 2009). The growth rate of mode II increases rapidly when S increases and/or H decreases moderately (Fig. 2d). From H150S100 to H145S105, it presents a La Niña–like mean state change with slightly stronger trade winds and shallower thermocline. Accordingly, the growth rate of mode II increases from below zero to $\sim 0.4\,\mathrm{yr}^{-1}$ (closed circle in Fig. 2d) while that of mode I increases from ~ 0.25 to $\sim 0.55\,\mathrm{yr}^{-1}$ as well (closed circle in Fig. 2b). The two modes both become unstable with comparable growth rates. The corresponding period of mode II increases slightly from 1.55 to 1.65 years while the period of mode I decreases from 4.2 to 3.7 years. When the mean state moves further to H140S110, the growth rates of mode I and II are $\sim 0.4\,\mathrm{yr}^{-1}$(square in Fig. 2b) and $\sim 1.3\,\mathrm{yr}^{-1}$ (square in Fig. 2d), respectively. Meanwhile, the period of the mode I (mode II) decreases to 3.3 years (increases to $\sim$1.8 years). At this mean state, the two modes are both unstable; however, the mode II rather than mode I becomes the dominant mode. With this type of mean state change, the corresponding changes in the instabilities of the two modes indicate that the La Niña–like mean state change would favor the fast-paced mode II as the dominant ENSO mode. It appears in qualitative agreement with the observed dominance of quasi-biennial ENSO oscillation after 2000 (Xie et al. 2015b). In addition, these findings are similar to the results of BJ08, although the relative changes in the mean states are different because of the altered standard mean state.

When the mean state changes from H150S100 to H140S90, the growth rate of mode I remains almost

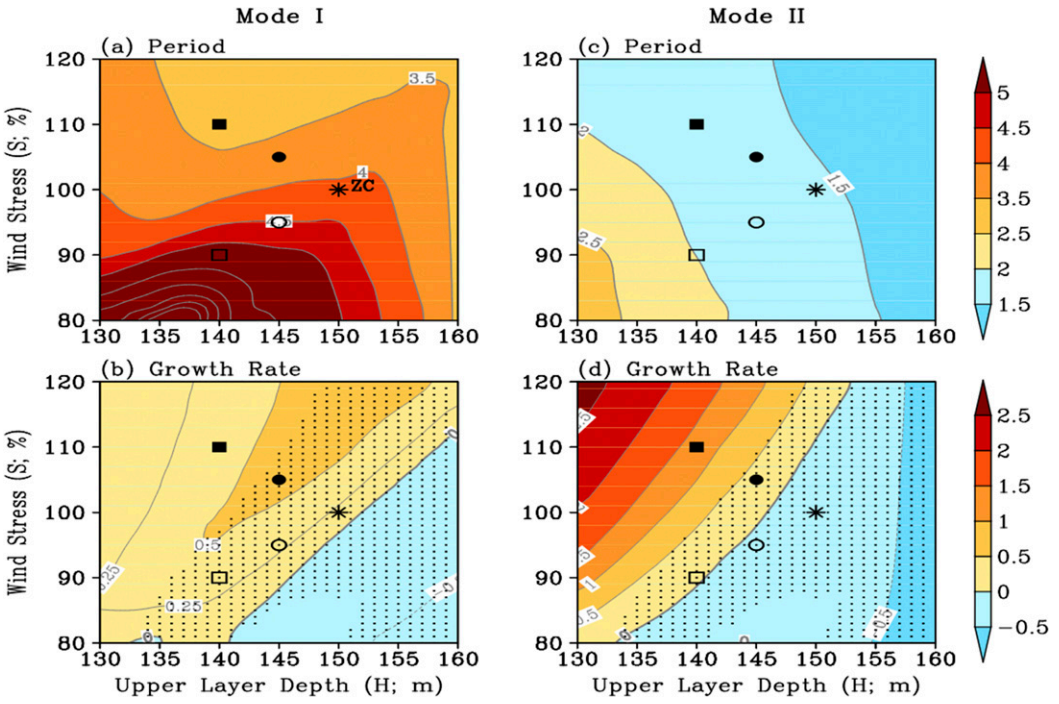

FIG. 2. Dependence of the (a) period (yr) and (b) growth rate (yr^{-1}) of the mode that has a period of around 4 yr (mode I) as a function of the mean wind stress intensity S and oceanic upper-layer depth H. (c),(d) As in (a),(b), but for the mode with a period of approximately 2 yr (mode II). The contour intervals of period and growth rate are 0.5 yr and 0.5 yr^{-1}, respectively, except in (b), where the contour interval is 0.25 yr^{-1} for a clearer illustration. The star represents the new standard mean state, and the circles and squares denote four additional mean states (see the text for details). The stippled areas in (b) and (d) indicate that the growth rate of mode I is greater than that of mode II.

unchanged (open symbols in Fig. 2b), while mode II gradually destabilizes and eventually becomes unstable (open symbols in Fig. 2d). The periods of both modes become longer (open symbols in Figs. 2a,c). This type of mean state corresponds to weaker trade winds, a weaker cold tongue, and a shallower thermocline. This kind of mean state is similar to the typical Pacific climate change in the global warming simulations (Vecchi et al. 2006; DiNezio et al. 2009; Yeh et al. 2009). Our results indicates that an increase in the CP ENSO activity as the CP mode (the mode II herein) becomes near critical in such a climate mean state, which appears to be consistent with the finding of increase CP ENSO activity under the simulated warm climates (Yeh et al. 2009). For the state-of-the-art climate models, it is still difficult to find a consensus in ENSO change even though they commonly simulate similar future mean state changes in the tropical Pacific climate (Collins et al. 2010; Stevenson 2012; Taschetto et al. 2014).

b. *Eigenstructures of the two ENSO modes*

Figures 3 and 4 show the eigenstructures of the SSTA of the two natural modes at the aforementioned five typical mean states. At these mean states, mode I shows an SSTA center in the Niño-3 region (5°S–5°N, 150°–90°W) (Fig. 3), which resembles the pattern of the observed EP El Niño event. Mode II has an SSTA center in the Niño-4 region (5°S–5°N, 160°E–150°W) with a weak SSTA extension in the eastern Pacific (Fig. 4), which is similar to the observed CP El Niño event. Therefore, we regard the two modes as the EP and CP ENSO modes. In fact, the present EP (CP) mode is basically the QQ (QB) mode in BJ08. Despite the fact that the entire eigenvectors for the model I and II are both normalized, the SSTA associated with the CP mode is naturally weaker than that with the EP mode. This indicates that for the same strength of SST anomalies, the oceanic currents and thermocline responses for CP ENSO mode should be stronger than those for EP ENSO. It should also be noted that the SSTA pattern of EP mode changes little whereas the SSTA center of CP mode shifts clearly as the mean state changes.

For a composite view, all the SSTA eigenvectors associated with each mode are composited following the evolving phases indicated by the Niño-3 or Niño-4 index. Phases 0 and 2π (π) are the phases when the index

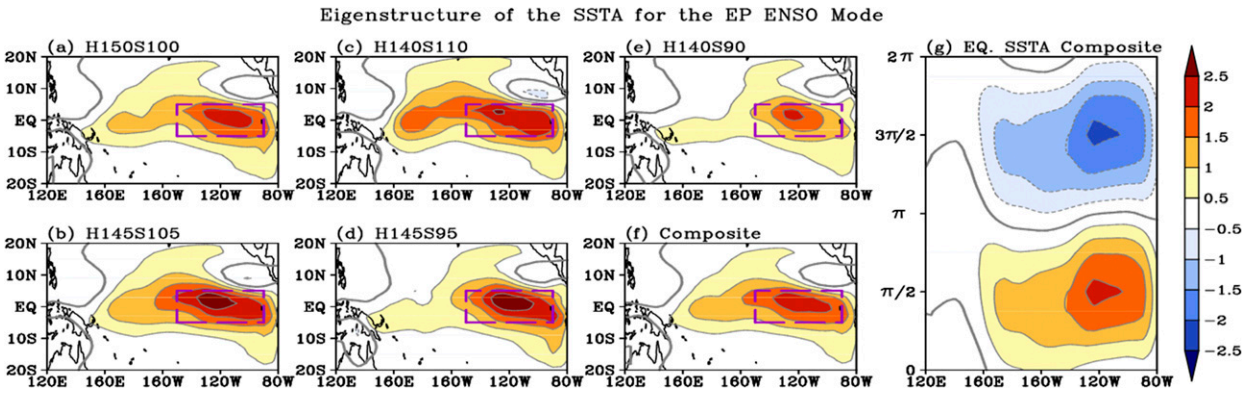

FIG. 3. (a)–(e) Eigenstructures of the mature SST anomalies (SSTAs) for the EP ENSO mode at the five mean states and (f) their composite. The superimposed purple boxes denote the Niño-3 region (5°S–5°N, 150°–90°W). (g) The composited life cycle of the equatorial SSTA (averaged between 3°S and 3°N). The life cycle is represented according to the evolutional phases indicated by the corresponding Niño-3 indices. Note that the EP mode is the second most unstable mode at H140S110.

ascend (descends) across zero, and phase $\pi/2$ ($3\pi/2$) is the time when the index reaches the positive (negative) peak. From the Hovmöller diagrams of the equatorial SSTA, the SSTA of the EP mode propagates eastward (Fig. 3g), whereas that of the CP mode propagates westward in the central-western Pacific and eastward in the eastern Pacific (Fig. 4g). The propagation of El Niño SSTA is related to the relative importance of the thermocline (TH) and zonal advective (ZA) feedbacks: it would propagate eastward if TH exceeds ZA, and propagate westward if otherwise (Jin and Neelin 1993a,b; FP01; Santoso et al. 2013).Therefore, the distinct propagations indicate that the two ENSO modes are controlled by different mechanisms. Detailed investigation on the dynamics of the two leading modes will be reported in the next context.

The eigenstructures of SSTA associated with the two leading modes at other mean state are similar to the typical pair shown above, even at some extreme mean states in the *H*–*S* space (Fig. 5). For example, at H130S80 where the mean wind stress is the weakest and thermocline is the shallowest among the entire mean states, the SSTA patterns associated with the two modes are still similar to the composite patterns (Figs. 5a,c). Interestingly, the SSTAs of both modes at H130S80 propagate eastward (Figs. 5b,d). It is consistent with the notion that the weakened mean currents (also weakened mean wind stress) would favor the occurrences of an eastward-propagating El Niño (Santoso et al. 2013). In fact, when the mean state is closer to the lower-left corner point of the *H*–*S* space, the eastward propagation of the SSTAs of the two modes are more obvious. However, at the mean states of H130S120 and H160S120 where the mean wind and mean ocean currents are very strong, the eastward propagations in the EP mode are very weak (Figs. 5f,j), whereas the westward propagations in the CP mode are remarkable (Figs. 5h,l). After all, despite significant changes in the

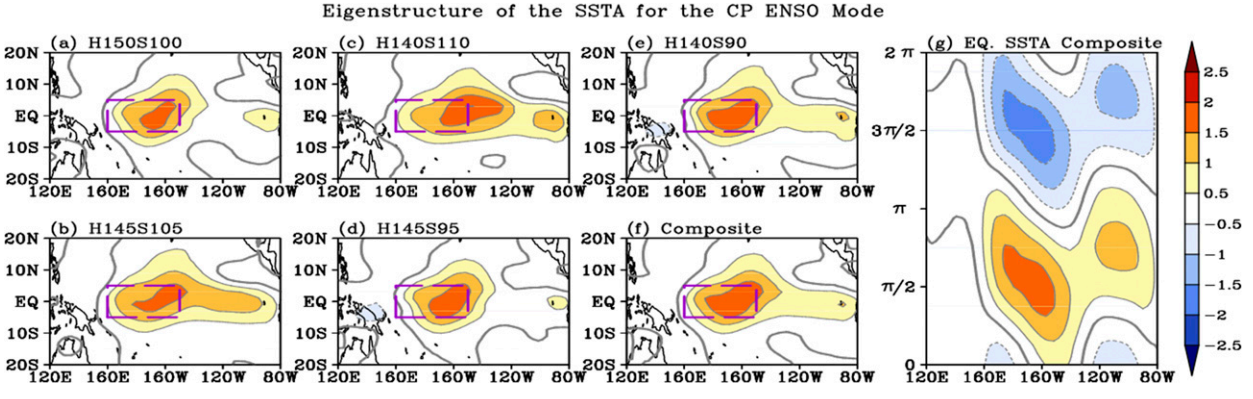

FIG. 4. As in Fig. 3, but for the CP ENSO mode. The superimposed purple boxes denote the Niño-4 region (5°S–5°N, 160°E–150°W). At H140S110, the CP mode is the first most unstable mode.

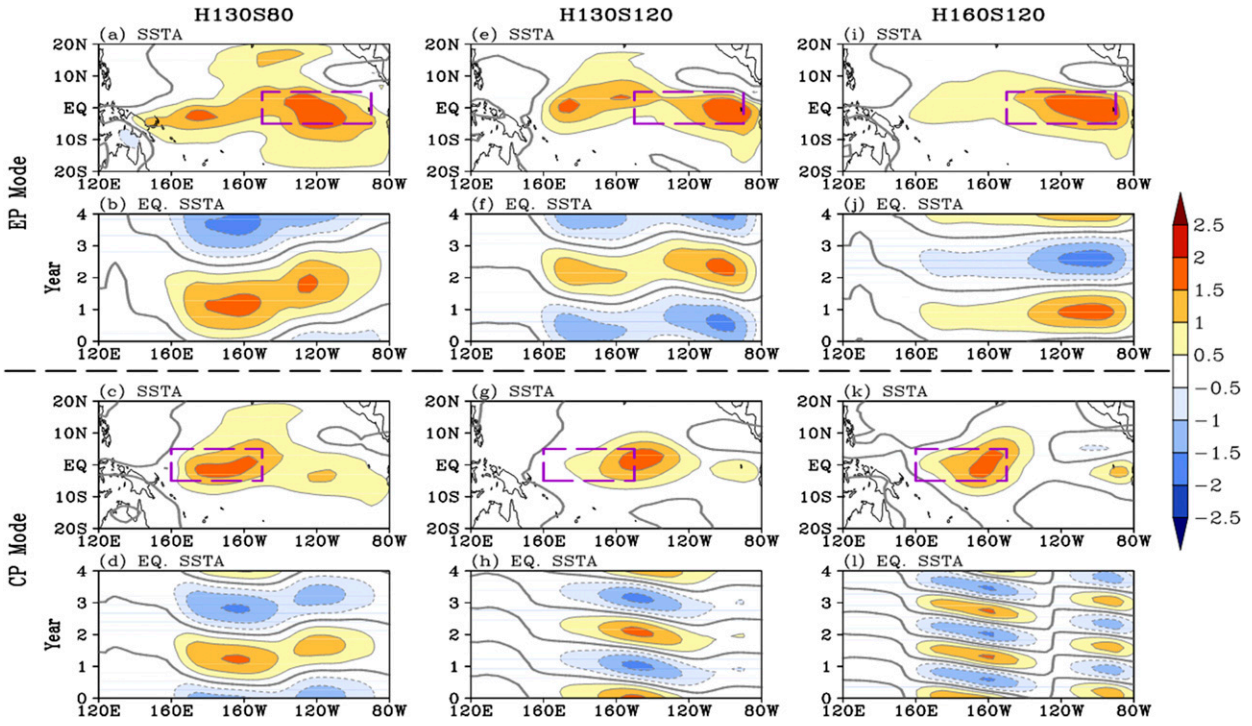

FIG. 5. Eigenstructures of the SSTA associated with the two ENSO modes at the three extreme mean states of H130S80, H130S120, and H160S120, and the evolutions of the equatorial SSTA. The top (bottom) panels show the EP (CP) ENSO mode, and the superimposed purple boxes in the top (bottom) panels denote the Niño-3 (Niño-4) regions. At H130S80 and H130S120, the CP (EP) is first most unstable mode.

mean state, the SSTA structures of the two modes are largely robust.

c. *Evolutions of the two leading ENSO modes*

We now further examine the evolutions of the equatorial SST, surface zonal wind, wave-induced currents (currents that are averaged between the surface and subsurface layers), and thermocline depth anomalies of the two modes. In the onset of warm phases of both modes, there are little SST and atmospheric wind anomalies (Figs. 6a,g). However, for the EP ENSO mode, unlike the calm surface, there are clearly positive thermocline depth anomalies in the western Pacific and along the entire equator, which are accompanied by eastward ocean current anomalies (Figs. 6b,h). For the CP ENSO mode, the equatorial thermocline depth anomalies are much weaker yet noticeable. Both of these patterns suggest recharged states of the warm pool oceanic heat content that are theoretically viewed as a precondition for El Niño events (Jin 1996, 1997a).

One feature to notice is that the CP mode in this phase is in a significantly less recharged state than EP mode, but they are both in strongly recharging states as well. The recharging states are characterized by the off-equatorial heat contents that will be carried to the equator later due to the equatorward mass/heat content flux convergence associated with the meridional component of quasigeostrophic ocean current anomalies. Another important feature to notice is that despite weak positive zonal uniform heat content in the CP mode at this stage, there are significant zonal current anomalies comparable with those of the EP mode, particularly in the western equatorial Pacific (Fig. 6h). As a consequence, these thermocline conditions will lead to enhanced equatorial heat content anomalies, and together with the strong positive zonal current, they will amplify the initial positive SST anomalies to grow into the strong positive phases for both modes. Recently, Newman et al. (2011) and Capotondi and Sardeshmukh (2015) identified strongly and weakly recharged heat content patterns as the optimal initial perturbations for the observed EP and CP El Niño events by using a linear inverse model (LIM) method. We notice that the thermocline patterns of the two modes at the onset phases are similar to the LIM optimal initial perturbations of the two types of ENSO events, except that the LIM initial thermocline depth pattern of the CP El Niño event are clearly negative in the far eastern Pacific. Moreover, the similarity between the initial SSTA patterns and the differences between the initial thermocline

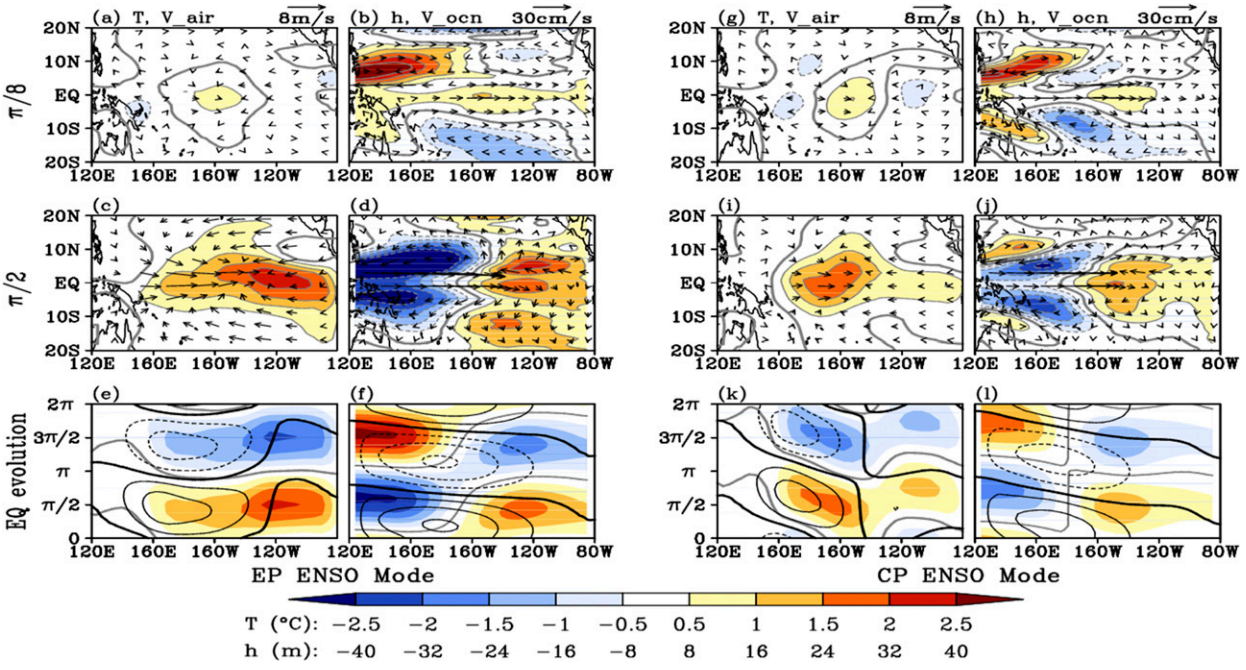

FIG. 6. Eigenvector fields of the two ENSO modes at the onset ($\pi/8$) and mature ($\pi/2$) phases, and in the completed life cycles. (a) The SST (shading) and surface wind (vectors) anomalies, and (b) the anomalous thermocline depth (shading) and wave-induced ocean current (vectors) at the onset phase of the EP ENSO mode. (c),(d) As in (a),(b), but for the mature phase. (e),(f) The temporal evolution of the equatorial fields (averaged between 3°S and 3°N) in the life cycle of the EP mode. The color shading (black contour) shows the SST and thermocline depth (zonal wind and ocean current) anomalies. (g)–(l) As in (a)–(f), but for the CP ENSO mode. All variables are the composites of the five mean states in Fig. 2.

patterns of the two modes also supports Capotondi and Sardeshmukh's (2015) finding that it is the different initial thermocline patterns rather than SSTA patterns alone that favor the generations of different ENSO types.

In the mature phase of the EP ENSO mode, positive SSTA occupies the entire central-to-eastern Pacific with its center located in the eastern Pacific, and the associated anomalous westerlies are to its west side (Fig. 6c). As the quasi-equilibrium response to such winds, the eastern Pacific thermocline deepens and the western Pacific thermocline shoals (Fig. 6d). Associated with anomalous pressure gradient forces induced by these thermocline fluctuations, anomalous eastward currents occur along the equator. It is noteworthy that the poleward current and positive thermocline depth anomalies are evident in the off-equatorial eastern Pacific beyond 5°, indicating that it has entered a strong heat content discharging state at the peak phase of the EP mode. In the peak phase of the CP mode, however, the largest SSTAs are confined in the central Pacific, which generates wind convergence near 150°W with strong westerly anomalies to the west side and weak easterly anomalies in the east side (Fig. 6i).The thermocline pattern is fairly similar to that of the EP mode, except that the positive center of equatorial thermocline shifts westward to about 140°W instead of 120°W as in the EP mode. Similar to the EP mode, the discharge of heat content in the CP mode is also evident, manifested by the weak but noticeable poleward quasigeostrophic current in the off-equatorial regions (Fig. 6j).

For both modes, SSTAs develop from the onset phase to the mature phase by the anomalous temperature advection by the mean upwelling (TH feedback) and anomalous eastward currents (ZA feedback) in the first quarters of the life cycles. The locations of the peak SSTA are determined by the dominant dynamical mechanism. If an ENSO mode is dominated by TH (ZA), the center of the mature SSTA will locate in the eastern (central) Pacific (FP01; BJ08). In general, the evolving patterns of the two ENSO modes in the surface and subsurface are fairly similar to those of the observed EP and CP El Niño identified by Kug et al. (2009). The main difference is that the CP mode herein shows a weak but clear recharge/discharge process, while the heat content recharge/discharge features were less evident in the observed CP El Niño. Some complex climate models can also capture the heat content recharge/discharge process in the simulated CP El Niño events. For instance, Capotondi (2013) found indications of

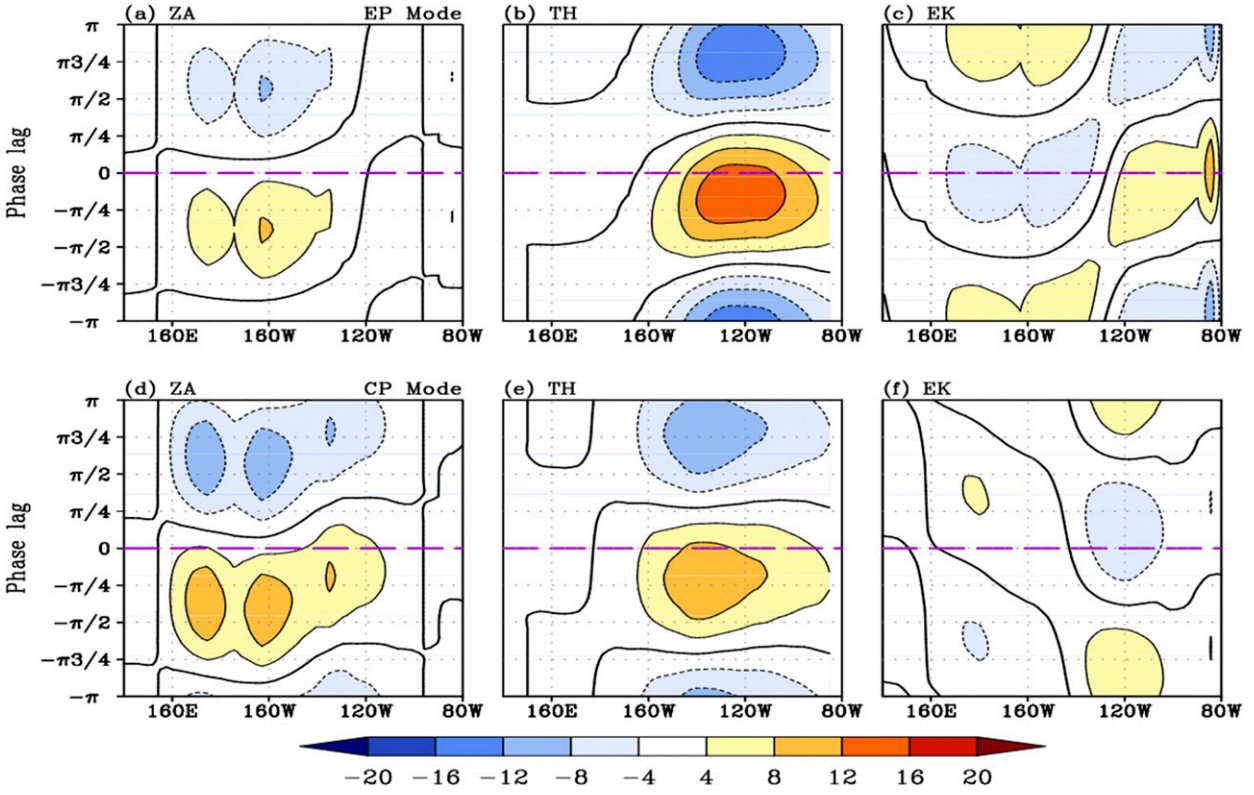

FIG. 7. Hovmöller diagrams of the contributions of the (a) zonal advective feedback (ZA), (b) thermocline feedback (TH), and (c) Ekman feedback (EK) to the SSTA growth of the EP ENSO mode. The phase lag "0" on the y axis corresponds to the peak phase. Negative (positive) lags are the phases before (after) the peak phase. The units are 0.01°C month^{-1}. (d)–(f) As in (a)–(c), but for the CP ENSO mode. The results are calculated from the composited variables of the five mean states in Fig. 2.

recharge/discharge process in the CP El Niño events with peak SSTAs in the Niño-4 region, but such indications disappeared in the events with the largest SSTAs farther west (near 160°W). In the observations, these processes may be contaminated by variability on decadal time scales. When focusing on the interannual time scales only, Ren and Jin (2013) and Xie et al. (2015a) also found clear recharge and discharge features in the life cycle of the CP El Niño. Therefore, we conclude that the present eigenmodes are in reasonable agreement with the observations on the interannual time scale.

d. *Linear heat budget analyses of the two leading modes*

We also conduct a simple linear heat budget analysis to quantify the relative importance of each positive feedback to the SSTA growth for the two leading modes. The SSTA tendency equation [Eq. (A7) in the appendix] is therefore simplified to focus on the ZA, TH, and EK feedbacks only, as expressed in Eq. (1). The other terms in the tendency equation mainly act as damping effects (An et al. 1999; Jin et al. 2006; Ren and Jin 2013).

The contributions to the SST tendency from the three main feedbacks are averaged over 3°S–3°N, and their temporal–longitudinal evolutions are shown in Fig. 7. For both modes, the contribution from EK is less than that from the two others. For the EP mode, the contribution from ZA to the SST tendency in the maximal SSTA region is smaller than that from TH in the same region. Conversely, the relative contributions from TH and ZA are reversed for the CP mode. Furthermore, the two feedbacks dominate in different regions: ZA acts mainly in the central and western Pacific (Figs. 7a,d), whereas TH serves in the eastern Pacific (Figs. 7b,e).

During the developing phases, ZA and TH feedbacks provide positive contributions to the SSTA growth from as early as $3\pi/4$ phases prior to the mature phases of both modes. Furthermore, the ZA feedback provides a negative SST tendency just after the mature phase (Figs. 7a,d), so ZA feedback initially contributes to the phase transitions of both modes. For the EK term, it acts as a positive contributor to the SSTA growth in the eastern Pacific and a negative contributor in the central Pacific (Fig. 7c) during the developing phases of the EP mode (during the phases of $-\pi/2$ and 0). But during the

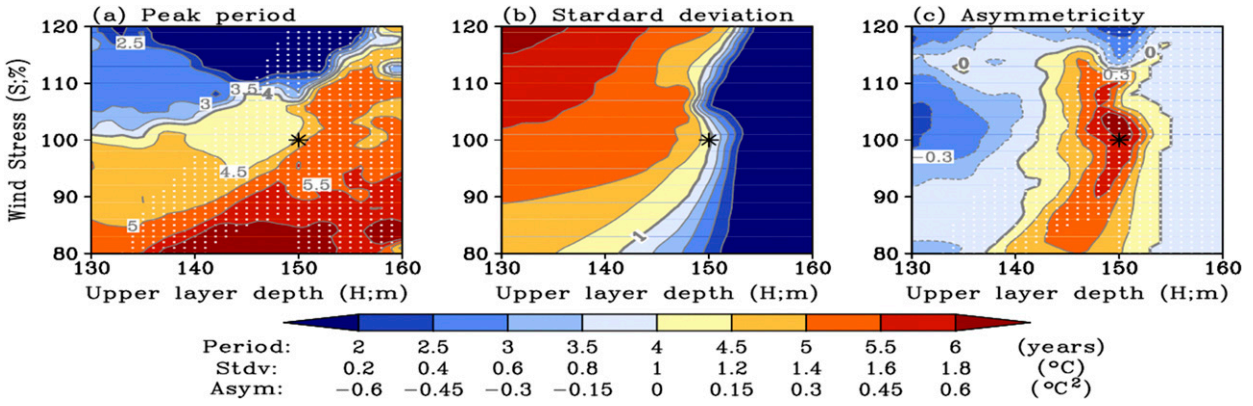

FIG. 8. (a) The peak period (yr), (b) standard deviation (°C), and (c) asymmetricity (°C^2) of the Niño-3.4 indices (SSTA averaged over 5°S–5°N, 170°–120°W) calculated from the last 900-yr segment of the 1000-yr nonlinear runs in the complete mean states. The stippled area in (a) and (c) indicates that the growth rate of the linear EP ENSO mode is greater than that of the CP ENSO mode.

CP mode's developing phase, the contribution from EK is negative (positive) in the eastern (central) Pacific (Fig. 7f). The patterns of the EK terms for the two modes are also similar to those found by Ren and Jin (2013, see their Figs. 8a,b).

Overall, the EP and CP modes are mainly controlled by the TH and ZA feedbacks respectively, although both ZA and TH feedbacks serve as two important positive contributors to the growths, and ZA provides the initial negative contribution for the phase transitions of the two leading modes. Our heat budget results are dynamically consistent with their different SSTA propagation features, and are also consistent with observational evidence (Ren and Jin 2013).

4. ENSO diversity in the nonlinear regimes

a. Simulated ENSO features in nonlinear solutions

In this section, we examine the nonlinear behaviors of the two leading modes by conducting a series of 1000-yr simulations under each mean state without the background annual cycle. Each integration starts with an imposed westerly anomaly in the western equatorial Pacific in the first four months as a kick off. The parameter settings are the same as those in section 3. We use the Niño-3.4 index (SSTAs averaged over 5°S–5°N, 170°–120°W) as a general index for the simulated ENSO events. The long-term mean of each Niño-3.4 index is removed. To exclude the influence from the initial wind stress forcing, only the data during the model year of 101–1000 are used in the following analysis.

The peak period, standard deviation, and asymmetricity of the Niño-3.4 index from the entire nonlinear integrations are calculated and shown in Fig. 8. The peak period is defined as the period with the largest power in the spectrum and meanwhile exceeds the 95% confidence level. In this study, the asymmetricity is defined as the variance-weighted skewness following An et al. (2005) and Hayashi and Watanabe (2017):

$$\text{asymmetricity} = \frac{m_3}{(m_2)^{1/2}}, \tag{3}$$

where m_k is the kth moment,

$$m_k = \sum_{i=1}^{N} \frac{(x_i - \overline{X})^k}{N},$$

and where x_i is the ith element, $\overline{X}$ is the mean, and N is the number of elements. Asymmetricity differs from skewness, which is normalized by denominator $(m_2)^{3/2}$. It is a good measure to quantify ENSO warm/cold asymmetry.

First of all, the Niño-3.4 index at the standard mean state H150S100 shows a major peak period of 4.6 years (Fig. 8a), a standard deviation of 0.94°C (Fig. 8b), which are all quite close to the corresponding observational values (4.2 years and 0.88°C) during 1980–2000. However, the asymmetricity herein (0.52°C^2) is greater than that from observation (0.34°C^2) during the same period, which indicates too strong warm/cold asymmetry in the model simulation.

As seen in Fig. 8a, the dependences of the peak period on the mean states show some similarities with the linear eigenperiods. The peak period generally decreases with the enhancement of the mean wind stress, which is also consistent with findings in Manucharyan and Fedorov (2014). In the regimes where the EP mode is the most unstable, the nonlinear peak periods are in general in the quasi-quadrennial or even longer band. Over the upper-left quadrant where the CP mode is clearly the most unstable, the peak periods are around the quasi-biennial band. However, in the regime where the two

modes are both unstable and have comparable growth rates, the peak periods do not necessarily match the eigenperiods of the modes with greater linear growth rates. In addition to the impact from the intensity of mean wind stress, the peak periods in our simulations are also influenced by the meridional structures of the wind stress anomalies in the central Pacific. With the increases of the mean wind stress, the meridional width of the zonal wind stress anomaly in the central Pacific decreases and the ENSO period decreases as well (see Fig. A2 in the appendix), and it is consistent with the conclusions in Kirtman (1997) and Capotondi et al. (2006). Furthermore, the nonlinear periods are longer than the corresponding eigenperiods of the dominant ENSO mode. These all indicate that the periodicity has been altered by nonlinearity. The question of how such adjustments occur will be addressed in detail in a forthcoming paper.

The standard deviation of the Niño-3.4 index increases toward the top-left corner of the H–S space (Fig. 8b), because the enhancements of the mean ocean currents and zonal SST gradient can support not only the instability of EP mode and, but more importantly, increase the instability of CP mode. Jointly, this leads to amplifying ENSO variability toward that regime. In contrast, at least one of two leading ENSO modes are damped in the regime where the oceanic upper-layer depth H is larger than 150 m and the mean wind stress is relatively weak, the ENSO variability is consequently small or insignificant. The asymmetry (Fig. 8c) shows that the positive asymmetry is confined at the mean states where the EP mode is more unstable than the CP mode, while the negative asymmetry occupies the ENSO regimes with a more unstable CP mode. The asymmetry also reflects the fact that in the nonlinear simulations the EP (CP), the El Niño event is generally larger (weaker) than the La Niña counterpart at the mean states that allow for a more unstable EP (CP) ENSO mode. A reason for the negative amplitude asymmetry is that there is an upper limit for the total SST (30°C) in the model, but there is no lower limit. The El Niño SSTA thus has a maximum that is determined by the mean SST, whereas the La Niña SSTA has less constraint in its growth.

b. *El Niño patterns diversity*

The original nonlinear version of the ZC-type model shows weak ability in producing the CP El Niño unless the model errors are corrected (Duan et al. 2014) or some additional parameterization of the westerly wind bursts is employed (Lian et al. 2014; Chen et al. 2015). However, with the presence of the two leading modes arguably of relevance to the observed El Niño flavors, we now examine how these linear modes may cause the diversity of ENSO patterns in the nonlinear simulations. We use a fuzzy clustering method to identify the different El Niño SSTA patterns. Only the El Niño events undergo the cluster analysis, because the simulated La Niña events in our MZC model are difficult to be divided into two types, which is consistent with the observed La Niña events being roughly in one group (e.g., Kug et al. 2009; Kug and Ham 2011; Chen et al. 2015). To focus on the El Niño events only, the Niño infinity (Niño$_\infty$) index proposed by Karnauskas (2013) is also used as a supplement of the Niño-3.4 index to capture all the El Niño events for the clustering analysis. The Niño$_\infty$ index is defined as follows:

$$\text{Niño}_\infty(t) = \overline{T'_{\varphi=0}(\lambda, t)} \text{ for } T' > 0, \tag{4}$$

where T' represents the SSTA, the overbar indicates the zonal mean 120°E $\le \lambda \le$ 80°W, and the subscript $\varphi = 0$ indicates meridional averaging 1°S $\le \varphi \le$ 1°N. Unlike the Niño-3.4 index that averages the SSTA signals in a fixed domain, the Niño$_\infty$ index collects the positive SSTA in the entire equatorial Pacific, so it is expected to identify the El Niño events with SSTA centers that are far beyond the Niño-3.4 region.

The fuzzy clustering method is an effective pattern-classification technique suitable for climate research (Kim et al. 2011; Chen et al. 2015). This method groups a set of given events into some specified categories based on their degree of membership, which is defined as the root-mean-square Euclidean distance to the cluster center. It does not require the predefined indices as criteria to divide the events into several groups. The detailed steps of applying this method to group El Niño clusters can be found in Chen et al. (2015).

We define an ''El Niño event'' as an event with its Niño-3.4 index larger than half of its standard deviation (Niño$_\infty$ larger than one standard deviation) for five consecutive months, and the mature phase of the event is defined as the month with the largest positive Niño-3.4 index in the five consecutive months. The Niño$_\infty$ index is not used to identify the mature phase because it has a phase lead–lag with the Niño-3.4 index (see Fig. 10). Then, centered at the mature phase, a 3-month mean of the SSTA is regarded as the mature El Niño pattern. In the stable ENSO regimes with weak ENSO variability, the Niño$_\infty$ index can identify some El Niño events missed by the Niño-3.4 index when the maximal SSTAs are centered beyond the Niño-3.4 region. The mature El Niño events will be identified into a specific cluster by the fuzzy clustering method. In this study, we set the cluster number as two rather than three, because we cannot identify an extreme El Niño cluster as in

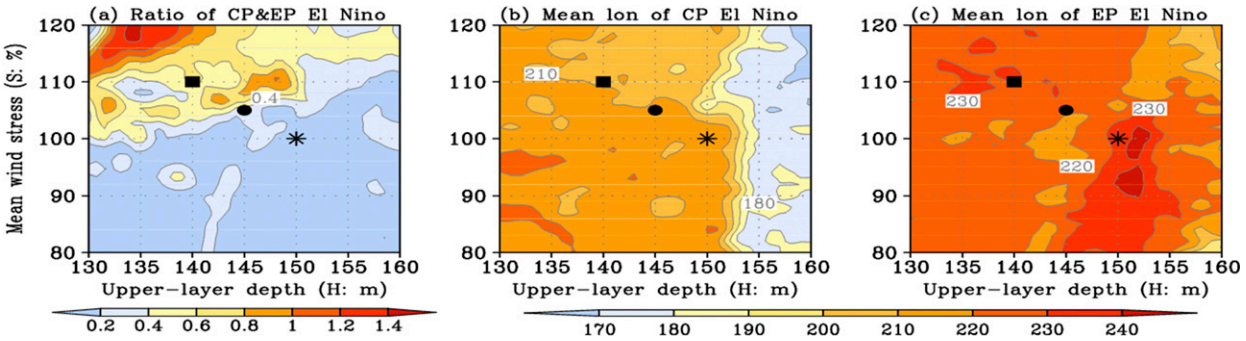

FIG. 9. Ratios of the identified CP and EP El Niño events in the last 900-yr segment from the 1000-yr nonlinear runs in the complete mean states. The star, filled circle, and filled square indicate the mean states of H150S100, H145S105, and H140S110, respectively.

Chen's study, and also because the identified El Niño clusters under three clusters show less distinctions (figure not shown) than those under two clusters (Fig. 11). For clarity, we name the El Niño cluster that shows SSTA center at a more eastern longitude as the EP El Niño cluster, and the cluster that has SSTA center located more westward as the CP El Niño cluster.

The occurrence ratios of the event numbers of the identified CP and EP El Niño clusters and their mean longitudes of maximal SSTAs are shown in Fig. 9. In general, the ratio increases toward the upper parts of *H*–*S* space (Fig. 9a), indicating that the occurrence of the CP El Niño increases with the enhancements of the mean wind stress and the shoaling of the thermocline. In particular, the CP/EP event ratio reaches its maximum around the top-left corner of the *H*–*S* space where the linear growth rate of the CP ENSO mode is near its maximum and that of the EP ENSO mode is near its positive minimum. Therefore, the ratios of CP and EP El Niño events in the nonlinear solutions are consistent with the relative sizes of the growth rates in the linear eigenanalysis. Because the ENSO period decreases toward the top-left corner of the *H*–*S* space (Fig. 8a) and meanwhile the CP/EP event ratio increases, the occurrence of the CP El Niño is more frequent while that of the EP El Niño is similar as in the standard cases. The mean longitudes of the maximal SSTAs of the two El Niño clusters show that the longitude of 140°W is a boundary to divide the two El Niño clusters at the mean states that supports at least one unstable ENSO mode (Figs. 9b,c). However, at the mean states where at least one ENSO mode is stable (when *H* is larger than 150 m and the standard deviation is very small), the two El Niño clusters are more distinguishable in the locations of maximal SSTAs: the weak CP El Niño is located near the date line while the weak EP El Niño center is east of 150°W. Overall, the SSTA centers of the two El Niño clusters are much closer than the SSTA centers in the eigenstructures of the two linear ENSO modes in the unstable ENSO regimes. This indicates that the nonlinearity or the ENSO modal interaction can alter the El Niño patterns.

To display the diverse ENSO behaviors in detail, we choose three typical mean states (H150S100, H145S105, and H140S110) as examples. According to the linear stability analysis, the three mean states represent three different ENSO regimes: the EP ENSO regime (H150S100), the EP–CP ENSO codevelopment regime (H145S105), and the CP ENSO dominant regime (H140S110). Figure 10 shows examples of the Niño-3.4 and Niño$_\infty$ indices in the three ENSO regimes in an arbitrarily chosen 100-yr segment (year 501–600) of the model integrations. The ENSO irregularity is produced fairly well in the three regimes, in particular in the last one where there are irregular alternations of strong and weak El Niño events (Fig. 10c). We will show later that these strong and weak El Niño events are of different types. Furthermore, the duration of the strong El Niño event is generally longer than that of the weak one, especially in the first two ENSO regimes (Figs. 10a,b). Besides, the duration of El Niño is generally shorter than that of La Niña, which is similar to, but not as evident as, the duration asymmetry in the observation (Okumura and Decer 2010). This deficiency may be partly related to the exclusion of the annual cycle and equatorial zonal wind events related to the MJO and westerly wind bursts that can modulate the development and decay of ENSO.

The El Niño clusters and the number of events in each individual cluster identified in the aforementioned 100-yr segment are shown in Fig. 11. It should be noted that the simulated ENSO variability in the entire 1000-yr integrations in each of the three ENSO regimes is quite stationary, so that any 100-yr subset captures the basic features of the two El Niño clusters quite well. In the three cases, the Niño-3.4 and Niño$_\infty$ indices identify identical El Niño events. At the EP ENSO regime (H150S100), the two clusters of El Niño show their maximum SSTAs in the Niño-3 and Niño-3.4 regions

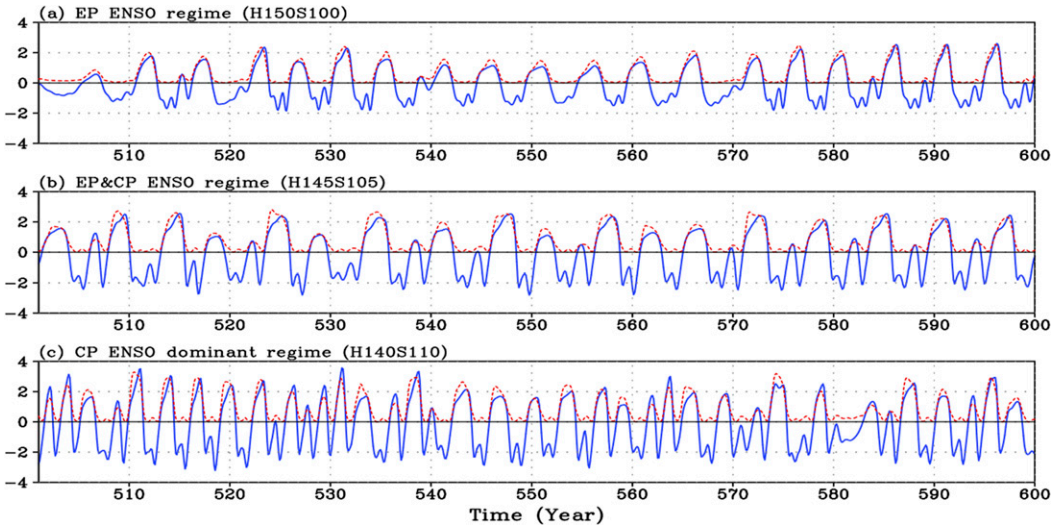

FIG. 10. Niño-3.4 indices of the model year 501–600 at the three ENSO regimes: EP ENSO (H150S100), EP–CP ENSO codevelopment (H145S105), and CP ENSO dominant (H140S100). The superimposed red dashed lines are the corresponding Niño_{∞} indices. See context for the definition of the Niño_{∞} index.

(Figs. 11a, b), respectively. The SSTA pattern of the EP El Niño cluster (Fig. 11a) resembles the eigenstructure of SSTA of the linear EP ENSO mode (see Fig. 3) and is also similar to the observed EP El Niño SSTA pattern. However, the CP El Niño cluster (Fig. 11b) shows less similarity to either the linear CP ENSO mode (see Fig. 4) or the observed CP El Niño in terms of the eastward-shifted SSTA center in this simulation. Even so, the two El Niño clusters are distinct from each other in the SSTA patterns and amplitudes. Moreover, the CP El Niño cluster shows weak warming in the eastern Pacific, which meets the important criterion proposed by Xiang et al. (2013) to separate the two types of El Niño. In addition, the member of the EP El Niño cluster are 4 times as large as those in the CP El Niño cluster, which is consistent with the notion that the EP mode rather than CP mode is the most unstable in this ENSO regime.

For the EP–CP codevelopment (H145S105) and CP dominant (H140S110) regimes, the patterns of the two El Niño clusters are similar to the clustered El Niño patterns in the EP ENSO regime (H150S100), but they have larger amplitudes (Figs. 11c–f). The members of the CP El Niño clusters at these two ENSO regimes increase in number, leading to increasing ratios of CP and EP El Niño events. This therefore indicates that the ENSO activities associated with the CP ENSO mode at these two ENSO regimes become more active than that in the EP ENSO regime because of enhanced instability

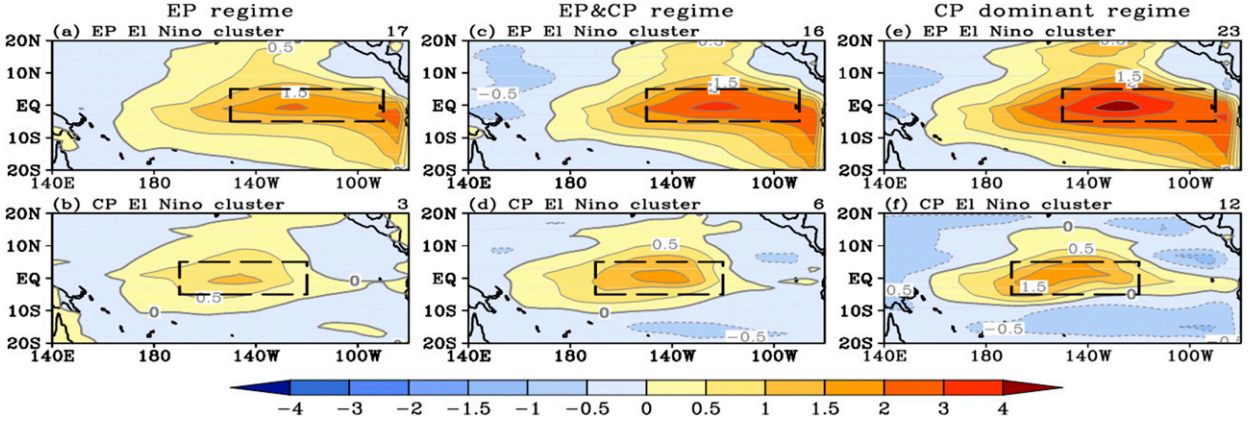

FIG. 11. Two identified El Niño patterns of the model year 501–600 at each of the three ENSO regimes. The patterns are identified using the fuzzy clustering method. The number of each cluster is shown in the top-right corner of each panel, and the dashed boxes denote (a), (c),(e) Niño-3 and (b),(d),(f) Niño-3.4 regions.

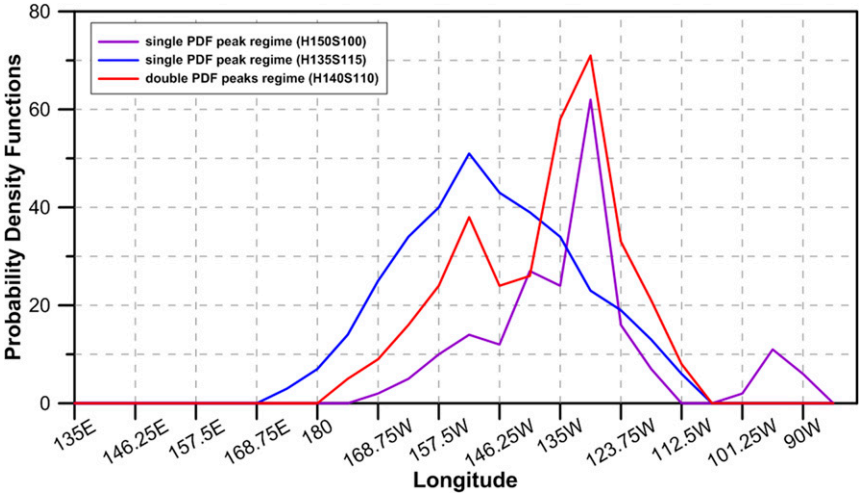

FIG. 12. Probability density functions (PDF) distributions of the mature SSTA centers in the nonlinear simulations during the model year 101–1000 in three kinds of ENSO regimes. The purple and blue curves indicate ENSO regimes showing single PDF peak, and the red curve denotes an ENSO regime with two PDF peaks.

of the CP ENSO mode. However, the number of the CP El Niño events is still smaller than that of the EP El Niño events even in the regime with the CP mode more unstable than the EP mode (Figs. 11e,f).

Despite the two distinguishable El Niño clusters, the probability density function (PDF) distributions of mature El Niño SST centers in our simulations do not always have two peaks. In the ENSO regime that is strongly dominated by one mode, there is only one PDF peak (Fig. 12). But in regimes where the EP mode is weakly unstable and the CP mode is more unstable (e.g., regime H140S110 in Fig. 11), there are two PDF peaks with a major peak in the east and a minor peak in a more westward longitude (Fig. 12). However, such types of double-peak distribution is in the limited regime because 1) the EP El Niño is much easier to emerge due to strong influence from the thermocline feedback, and 2) the modal interaction and nonlinearity can modulate the occurrence frequency of CP El Niño events. This favoritism of the EP El Niño events appears owing to the nonlinearity of the model. The nonlinear selection mechanism for the EP mode may be sensitive to the formulation of thermocline nonlinearity in the ZC model, and will be reported in future studies.

To confirm that the two El Niño clusters in our simulation are distinct types in their dynamics, we perform a simple heat budget analysis to the mixed layer SSTA to identify the major triggering mechanisms. Table 1 shows the surface layer heat budget terms averaged in the box of each El Niño cluster in Fig. 11 during a 6-month period before the peak phase. Only the terms of SST tendency, TH and ZA feedbacks are shown. For the EP El Niño clusters, TH is clearly the dominant contributor to the SST tendency, although ZA also contributes. For the CP El Niño clusters, however, the contribution from ZA exceeds that from TH. These results are consistent with our linear solutions and the observations as well. Therefore, there exist at least two types of El Niño events in our MZC model that show distinct differences in terms of spatial patterns, periods, amplitudes, and dynamical mechanisms in a similar manner as in the linear eigenanalysis and observations.

5. Conclusions and discussion

In this study, we employ a modified version of the Zebiak–Cane model with updated mean states to illustrate that the air–sea interactions in the tropical Pacific can give rise to two leading ENSO-like oscillatory modes. One is a low-frequency EP ENSO-like mode with a SSTA center in the eastern Pacific with a typical period between 3.5 and 8 years. The other mode is a CP ENSO-like mode with the maximum SSTA centered

TABLE 1. Surface layer heat budget terms in the developing stage (°C month^{-1}). The terms are averaged over the boxes indicated in Fig. 11 for the members in each cluster and in a 6-month window before an event reaches its peak.

	H150S100		H145S105		H140S110	
	Cluster 1	Cluster 2	Cluster 1	Cluster 2	Cluster 1	Cluster 2
dT/dt	0.313	0.171	0.437	0.194	0.538	0.236
TH	0.415	0.126	0.608	0.136	0.727	0.195
ZA	0.133	0.225	0.217	0.309	0.291	0.319

more toward the central Pacific and it oscillates on time scales of 1.5–3 years. Within a broad range of mean states, the two ENSO modes are robust and can coexist. In general, the two modes are more unstable when the mean wind stress increases. However, they show different sensitivities to the changes in the oceanic upper-layer depth. The CP ENSO mode dominates the ENSO mode when the upper-layer ocean becomes shallower, while the EP ENSO mode is the dominant mode if the upper-layer ocean becomes deeper.

The air–sea coupling processes during the life cycles of the two modes are somewhat similar in the surface fields, but different in the subsurface. For both modes, the initial SSTAs start in the central Pacific with weak wind anomalies. However, in the subsurface layer, there are clear heat content recharged states and eastward ocean current anomalies. The heat content recharged state in the EP mode is strong and basinwide, while it is weak and confined in the central-western Pacific in the CP mode. However, the eastward ocean current anomalies for the CP mode are more basinwide and even stronger than the EP mode in the western Pacific. These subsurface states lead to amplifications of the initial SSTAs by TH and ZA feedbacks in the first quadrant of the life cycles of the two modes. The linear heat budget analysis consistently reveals that the EP mode is strongly controlled by TH, whereas the CP mode shows more importance for ZA. Furthermore, ZA also provides the primary negative contribution for phase transitions of both modes. These findings are consistent with the observational evidences from Ren and Jin (2013) and Xie et al. (2015b).

In the nonlinear simulations, the peak period matches the eigenperiod of the more unstable ENSO mode at most of the entire mean states. The ENSO amplitude (standard deviation) increases toward the regime where the CP mode is increasingly unstable, partly because of enhanced ENSO instability and partly because of increased mean ocean currents. It seems different from the observed ENSO amplitude reduction in the recent decade when the CP El Niño dominates. It is because of that the increased ENSO amplitude in the nonlinear simulation is contributed to by 1) the enhanced EP ENSO events that still occur frequently and 2) the increased occurrence and amplitude of CP ENSO events in this regime. ENSO asymmetry changes gradually from positive to negative when ENSO regime moves from the EP ENSO regime toward the CP ENSO-dominated regime. It indicates that EP El Niño is generally stronger than EP La Niña while CP El Niño is generally weaker than EP La Niña. Two types of El Niño events can co-occur in some ENSO regimes, which supports at least one type of unstable ENSO modes. The two El Niño types differ from each other in terms of peak SSTA patterns and dynamic mechanisms. The ratio of CP–EP El Niño event numbers increases as the instability of the CP ENSO mode increases.

Recent studies have suggested a number of mechanisms as the potential sources for the different types of ENSO. Multiplicative atmospheric forcing, such as the westerly wind bursts (WWBs) and nonlinear advection, have been suggested to be important for the two main El Niño types (Chen et al. 2015; Chen and Majda 2016, 2017; Hayashi and Watanabe 2017). In addition, Capotondi and Sardeshmukh (2015) reported that different initial subsurface thermocline conditions may lead to the occurrences of two types of El Niño. Our study suggests that the instabilities of the two leading ENSO modes of relevance to the two types of El Niño events are essential to the simulated diverse events. Because multiplicative noise forcing can directly alter ENSO stability (Jin et al. 2007), and nonnormal growth may be triggered by optimal initial perturbations for specific type of events, these mechanisms therefore may all contribute. Further studies, in particular to examine their relative importance may help us to understand the main sources and fundamental mechanisms for the ENSO pattern diversity and temporal complexity.

Acknowledgments. R. Xie is supported by the National Natural Science Foundation of China (NFSC Grant 41506017), the National Programme on Global Change and Air-Sea Interaction (GASI-IPOVAI-06), and the NSFC–Shandong Joint Fund for Marine Science Research Centers (U1406402). F.-F. Jin is supported by the U.S. National Science Foundation (NSF) Grant AGS-1406601, and U.S. Department of Energy Grant DE-SC0005110. F.-F. Jin is also supported for an extended visit by IBS Center of Climate Physics (ICCP) at Pusan National University of Korea. The observational and reanalysis data used in this study are provided by the NOAA/OAR/ESRL PSD, Boulder, Colorado, from their website at http://www.esrl.noaa.gov/psd/. The authors thank Drs. A. Timmerman and J.-S. Kug for stimulating discussions, and Dr. Kris Karnauskas and two anonymous reviewers for their insightful comments and suggestions on the earlier version of this manuscript that improved the quality of the final paper.

APPENDIX

The Modified Zebiak–Cane Model

a. Equations of the new atmospheric component

The governing equations for the atmospheric model are similar as those in ZC87, but they differ in three terms: the inclusion of cumulus moment transport

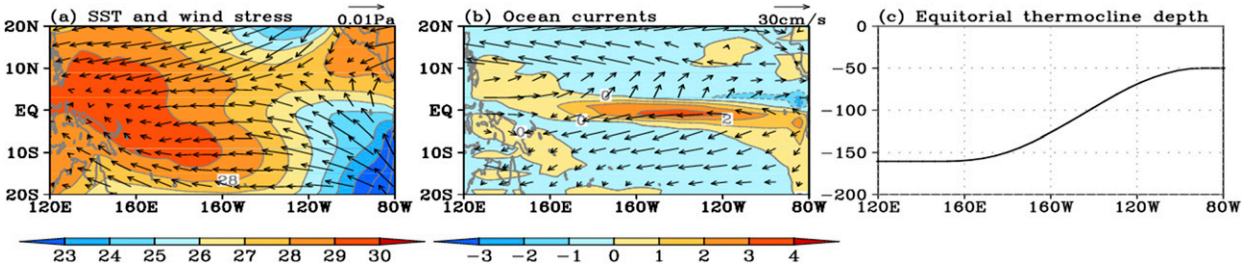

FIG. A1. Spatial patterns of (a) SST (°C, shaded) and wind stress (Pa, vectors), (b) oceanic vertical current (10^{-5} m s^{-1}, shaded) and horizontal currents (cm s^{-1}, vectors), and (c) thermocline depth (m) along the equator at the standard mean states (H150S100).

(CMT) in the zonal moment equation, the inclusion of an atmospheric heating efficiency factor that depends on the total states of SST and low-level convergence, and the slightly reduced wind convergence feedback. These modifications can help to suppress the unreasonable and broad wind responses in the eastern Pacific, but only cause minor changes in the central and western Pacific. Interested readers can find the detailed modifications and improvements in Xie et al. (2015b).

At iteration n, the equations are as follows:

$$\varepsilon u_a^n - \beta_0 y v_a^n = -(p^n/\rho_0)_x + A\overline{U}_z c^n, \tag{A1}$$

$$\varepsilon v_a^n + \beta_0 y u_a^n = -(p^n/\rho_0)_y, \tag{A2}$$

$$\varepsilon(p^n/\rho_0) + c_a^2[(u_a^n)_x + (v_a^n)_y] = \delta(-\dot{Q}_s - \dot{Q}_1^{n-1}), \tag{A3}$$

$$\dot{Q}_s = (\alpha T)\exp[(\overline{T} - 30)/16.7], \tag{A4}$$

$$\dot{Q}_1^n = \beta_1[M(\overline{c} + c^n) - M(\overline{c})]. \tag{A5}$$

where the following terms are the modifications: $A\overline{U}_z c^n$ in Eq. (A1), δ in Eq. (A3), and β in Eq. (A5). Here, the original Heaviside function $M(x)$ is redefined and replaced by a new form listed in Eq. (A9). In the CMT term ($A\overline{U}_z c^n$) in Eq. (A1), A (=0.003) is a nondimensional constant that measures the efficiency of CMT for unit convergence anomaly, and $\overline{U}_z$ ($=\overline{U}_{200} - \overline{U}_{925}$) is the climatological vertical zonal wind shear between 200 and 925 hPa. In this way, CMT can provide additional westerly (easterly) anomalies at the low level when anomalous low-level convergence (divergence) is induced. The heating efficiency factor δ is empirically designed on an observational basis, and it is expressed as follows:

$$\delta = \begin{cases} 1, \text{ if } T_s \geq 27.5°\text{C and } C \geq 0, \\ (T_s - 25.5) \times 0.4 + 0.2, \text{ if } 25.5° \leq T_s < 27.5°\text{C} \\ \text{and } C \geq 0, \\ 0.2, \text{ otherwise}. \end{cases} \tag{A6}$$

Here, T_s is the total SST (the sum of the mean and anomalous SST), and C is the total low-level wind convergence. This parameter has little influence on the heating anomalies in the western and some parts of the central Pacific, while it can reduce a large number of unreasonable heating anomalies in the eastern Pacific where the total SST is relatively lower and the low-level winds are still divergent even during some El Niño events. Parameter β_1 measures the strength of wind convergence feedback, and in our version its nondimensional value is reduced from 0.75 to 0.6 to reduce the heating anomalies.

The three terms reduce the wind response in the eastern Pacific. The heating efficiency factor δ and the reduced convergence feedback parameter β_1 can reduce the heating anomalies, in particular in the eastern Pacific, leading to weaker atmospheric wave and wind responses; and CMT provides additional winds to compensate for the momentum loss caused by the reduction in the heating anomalies. As a result, the atmospheric model can better simulate the ENSO wind anomalies [see Fig. 9 in Xie et al. (2015b)].

b. *Some equations and parameters of the ocean model*

Here, we list some equations and parameters of the ocean model that are mentioned in this study for a better understanding.

1) The surface-layer temperature tendency equation:

$$\frac{\partial T}{\partial t} = -\mathbf{u}_1 \cdot \nabla(\overline{T} + T) - \overline{\mathbf{u}}_1 \cdot \nabla T - [M(\overline{w_s} + w_s) - M(\overline{w_s})]\frac{d\overline{T}}{dz} - M(\overline{w_s} + w_s)\frac{dT}{dz} - \alpha_s T, \tag{A7}$$

where the overbar means the climatological mean state, $\mathbf{u}_1$ is the surface layer currents, w_s is the vertical velocity at the bottom of the surface layer, and α_s is the linear damping rate. Here $M(x)$ is a newly defined function in Eq. (A9).

2) The entrainment efficiency γ is used to measure the mixing efficiency of the subsurface (T_{sub}) and surface (T) temperature anomalies to influence the

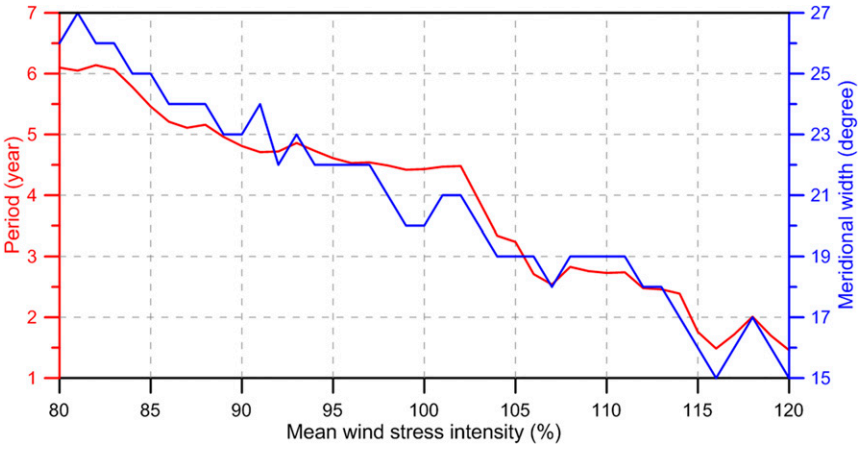

FIG. A2. Dependence of ENSO period (red line) on the meridional width of the zonal wind stress anomalies (blue line) in the nonlinear simulations with a constant H (140 m) and varying S from 80% to 120% of the reference intensity. See the text in the appendix for the definition of the meridional width.

temperature at the bottom of surface layer (T_e). It is expressed as

$$T_e = \gamma T_{\text{sub}} + (1 - \gamma)T. \tag{A8}$$

3) The function $M(x)$ is replaced by a new function that is smoother than the original Heaviside function when x changes from negative to positive. Its new definition follows the form in Bejarano (2006) as follows:

$$M(x) = 0.5 \times x \times [\tanh(x/a) + 1]. \tag{A9}$$

In Bejarano (2006), a small value of a was chosen to ensure that the hyperbolic tangent function approached the Heaviside function used by the original ZC formulation. The hyperbolic tangent function avoids the discontinuity arising from differentiating the Heaviside function numerically in the linearization. Therefore, the typical value of a in the atmospheric model is set to 10% of the atmospheric convergence, and that in the oceanic model is set to 10% of the upwelling.

After the modified model is finalized, the reference wind stresses are updated to the mean during 1980–2000 to spin up the ocean model, and new ocean currents are produced. Figure A1 shows the annual mean SST, wind stresses, three-dimensional ocean currents, and the equatorial thermocline depth in the updated standard mean state.

c. *The ENSO period and the meridional width of the zonal wind stress anomalies in the central Pacific*

In addition to the impact from the intensity of the mean wind stress prescribed to the model, the ENSO period in the nonlinear simulation is also influenced by the meridional width of the wind stress anomalies in the central Pacific, as revealed by Kirtman (1997) and Capotondi et al. (2006). Here, the zonal wind stress anomalies are regressed onto the Niño-3.4 index, and the meridional width of the wind response is defined as the meridional extension of the westerly wind stress anomalies averaged in the Niño-4 region. Figure A2 shows that in the cases with $H = 140$ m and S varying from 80% to 120% of the reference intensity, the meridional widths of the wind anomalies in the central Pacific decrease from 27° to 15°, and ENSO periods decrease from 6.0 to 1.5 years. It indicates a high influence from the spatial structure of the wind stress anomalies to the ENSO period, with meridionally broader anomalies leading to a longer ENSO period.

REFERENCES

An, S.-I., and F.-F. Jin, 2000: An eigen analysis of the interdecadal changes in structure and frequency of ENSO mode. *Geophys. Res. Lett.*, **27**, 2573–2576, https://doi.org/10.1029/1999GL011090.

——, and ——, 2001: Collective role of zonal advective and thermocline feedbacks in the ENSO mode. *J. Climate*, **14**, 3421–3432, https://doi.org/10.1175/1520-0442(2001)014<3421:CROTAZ>2.0.CO;2.

——, ——, and I.-S. Kang, 1999: The role of zonal advection feedback in phase transition and growth of ENSO in the Cane-Zebiak model. *J. Meteor. Soc. Japan*, **77**, 1151–1160, https://doi.org/10.2151/jmsj1965.77.6_1151.

——, Y.-G. Ham, J.-S. Kug, F.-F. Jin, and I.-S. Kang, 2005: El Niño–La Niña asymmetry in the Coupled Model Intercomparison Project simulations. *J. Climate*, **18**, 2617–2627, https://doi.org/10.1175/JCLI3433.1.

Ashok, K., S. K. Behera, S. A. Rao, H. Weng, and T. Yamagata, 2007: El Niño Modoki and its possible teleconnections.

J. Geophys. Res., **112**, C11007, https://doi.org/10.1029/2006JC003798.

Battisti, D. S., 1988: Dynamics and thermodynamics of a warming event in a coupled tropical atmosphere–ocean model. *J. Atmos. Sci.*, **45**, 2889–2919, https://doi.org/10.1175/1520-0469(1988)045<2889:DATOAW>2.0.CO;2.

Bejarano, L., 2006: Coexistence of leading equatorial coupled modes for ENSO. Ph.D. dissertation, Florida State University, 118 pp., http://diginole.lib.fsu.edu/islandora/object/fsu:175766/datastream/PDF/view.

——, and F.-F. Jin, 2008: Coexistence of equatorial coupled modes of ENSO. *J. Climate*, **21**, 3051–3067, https://doi.org/10.1175/2007JCLI1679.1.

Capotondi, A., 2013: ENSO diversity in the NCAR CCSM4 climate model. *J. Geophys. Res. Oceans*, **118**, 4755–4770, https://doi.org/10.1002/jgrc.20335.

——, and P. D. Sardeshmukh, 2015: Optimal precursors of different types of ENSO events. *Geophys. Res. Lett.*, **42**, 9952–9960, https://doi.org/10.1002/2015GL066171.

——, A. Wittenberg, and S. Masina, 2006: Spatial and temporal structure of Tropical Pacific interannual variability in 20th century coupled simulations. *Ocean Modell.*, **15**, 274–298, https://doi.org/10.1016/j.ocemod.2006.02.004.

——, and Coauthors, 2015: Understanding ENSO diversity. *Bull. Amer. Meteor. Soc.*, **96**, 921–938, https://doi.org/10.1175/BAMS-D-13-00117.1.

Chen, D., and Coauthors, 2015: Strong influence of westerly wind bursts on El Niño diversity. *Nat. Geosci.*, **8**, 339–345, https://doi.org/10.1038/ngeo2399.

Chen, N., and A. J. Majda, 2016: Simple dynamical models capturing the key features of the Central Pacific El Niño. *Proc. Natl. Acad. Sci. USA*, **113**, 11 732–11 737, https://doi.org/10.1073/pnas.1614533113.

——, and ——, 2017: Simple stochastic dynamical models capturing the statistical diversity of El Niño Southern Oscillation. *Proc. Natl. Acad. Sci. USA*, **114**, 1468–1473, https://doi.org/10.1073/pnas.1620766114.

Collins, M., and Coauthors, 2010: The impact of global warming on the tropical Pacific Ocean and El Niño. *Nat. Geosci.*, **3**, 391–397, https://doi.org/10.1038/ngeo868.

DiNezio, P. N., A. C. Clement, G. A. Vecchi, B. J. Soden, B. P. Kirtman, and S.-K. Lee, 2009: Climate response of the equatorial Pacific to global warming. *J. Climate*, **22**, 4873–4892, https://doi.org/10.1175/2009JCLI2982.1.

Duan, W., B. Tian, and H. Xu, 2014: Simulations of two types of El Niño events by an optimal forcing vector approach. *Climate Dyn.*, **43**, 1677–1692, https://doi.org/10.1007/s00382-013-1993-4.

Fedorov, A. V., and S. G. Philander, 2000: Is El Niño changing? *Science*, **288**, 1997–2002, https://doi.org/10.1126/science.288.5473.1997.

——, and ——, 2001: A stability analysis of tropical ocean–atmosphere interactions: Bridging measurements and theory for El Niño. *J. Climate*, **14**, 3086–3101, https://doi.org/10.1175/1520-0442(2001)014<3086:ASAOTO>2.0.CO;2.

Furtado, J. C., E. Di Lorenzo, B. T. Anderson, and N. Schneider, 2012: Linkages between the North Pacific Oscillation and central tropical Pacific SSTs at low frequencies. *Climate Dyn.*, **39**, 2833–2846, https://doi.org/10.1007/s00382-011-1245-4.

Giese, B. S., and S. Ray, 2011: El Niño variability in simple ocean data assimilation (SODA), 1871–2008. *J. Geophys. Res.*, **116**, C02024, https://doi.org/10.1029/2010JC006695.

Gill, A. E., 1980: Some simple solutions for heat induced tropical circulation. *Quart. J. Roy. Meteor. Soc.*, **106**, 447–462, https://doi.org/10.1002/qj.49710644905.

Guilyardi, E., P. Braconnot, F.-F. Jin, S.-T. Kim, M. Kolasinski, T. Li, and I. Musat, 2009: Atmosphere feedbacks during ENSO in a coupled GCM with a modified atmospheric convection scheme. *J. Climate*, **22**, 5698–5718, https://doi.org/10.1175/2009JCLI2815.1.

Hayashi, M., and M. Watanabe, 2017: ENSO complexity induced by state dependence of westerly wind events. *J. Climate*, **30**, 3401–3420, https://doi.org/10.1175/JCLI-D-16-0406.1.

Jin, F.-F., 1996: Tropical ocean-atmosphere interaction, the Pacific cold tongue, and the El Niño Southern Oscillation. *Science*, **274**, 76–78, https://doi.org/10.1126/science.274.5284.76.

——, 1997a: An equatorial ocean recharge paradigm for ENSO. Part I: Conceptual model. *J. Atmos. Sci.*, **54**, 811–829, https://doi.org/10.1175/1520-0469(1997)054<0811:AEORPF>2.0.CO;2.

——, 1997b: An equatorial ocean recharge paradigm for ENSO. Part II: A stripped-down coupled model. *J. Atmos. Sci.*, **54**, 830–847, https://doi.org/10.1175/1520-0469(1997)054<0830:AEORPF>2.0.CO;2.

——, and J. D. Neelin, 1993a: Modes of interannual tropical ocean–atmosphere interaction—A unified view. Part I: Numerical results. *J. Atmos. Sci.*, **50**, 3477–3503, https://doi.org/10.1175/1520-0469(1993)050<3477:MOITOI>2.0.CO;2.

——, and ——, 1993b: Modes of interannual tropical ocean–atmosphere interaction–A unified view. Part III: Analytical results in fully coupled cases. *J. Atmos. Sci.*, **50**, 3523–3540, https://doi.org/10.1175/1520-0469(1993)050<3523:MOITOI>2.0.CO;2.

——, ——, and M. Ghil, 1996: El Niño/Southern Oscillation and the annual cycle: Subharmonic frequency-locking and aperiodicity. *Physica D*, **98**, 442–465, https://doi.org/10.1016/0167-2789(96)00111-X.

——, S. T. Kim, and L. Bejarano, 2006: A coupled-stability index for ENSO. *Geophys. Res. Lett.*, **33**, L23708, https://doi.org/10.1029/2006GL027221.

——, L. Lin, A. Timmermann, and J. Zhao, 2007: Ensemble-mean dynamics of the ENSO recharge oscillator under state-dependent stochastic forcing. *Geophys. Res. Lett.*, **34**, L03807, https://doi.org/10.1029/2006GL027372.

Kanamitsu, M., W. Ebisuzaki, J. Woollen, S.-K. Yang, J. J. Hnilo, M. Fiorino, and G. L. Potter, 2002: NCEP–DOE AMIP-II reanalysis (R-2). *Bull. Amer. Meteor. Soc.*, **83**, 1631–1643, https://doi.org/10.1175/BAMS-83-11-1631.

Kang, I.-S., J.-S. Kug, S.-I. An, and F.-F. Jin, 2004: A near-annual Pacific Ocean basin mode. *J. Climate*, **17**, 2478–2488, https://doi.org/10.1175/1520-0442(2004)017<2478:ANPOBM>2.0.CO;2.

Kao, H. Y., and J. Y. Yu, 2009: Contrasting eastern Pacific and central Pacific types of ENSO. *J. Climate*, **22**, 615–632, https://doi.org/10.1175/2008JCLI2309.1.

Karnauskas, K. B., 2013: Can we distinguish canonical El Niño from Modoki? *Geophys. Res. Lett.*, **40**, 5246–5251, https://doi.org/10.1002/grl.51007.

Kim, D., J.-S. Kug, I.-S. Kang, F.-F. Jin, and A. Wittenberg, 2008: Tropical Pacific impacts of convective momentum transport in the SNU coupled GCM. *Climate Dyn.*, **31**, 213–226, https://doi.org/10.1007/s00382-007-0348-4.

Kim, H.-S., C.-H. Ho, J.-H. Kim, and P.-S. Chu, 2011: Pattern classification of typhoon tracks using the fuzzy *c*-means clustering method. *J. Climate*, **24**, 488–508, https://doi.org/10.1175/2010JCLI3751.1.

Kirtman, B., 1997: Oceanic Rossby wave dynamics and the ENSO period in a coupled model. *J. Climate*, **10**, 1690–1704, https://doi.org/10.1175/1520-0442(1997)010<1690:ORWDAT>2.0.CO;2.

Kug, J.-S., and Y.-G. Ham, 2011: Are there two types of La Nina? *Geophys. Res. Lett.*, **38**, L16704, https://doi.org/10.1029/2011GL048237.

——, F.-F. Jin, and S.-I. An, 2009: Two types of El Niño events: Cold tongue El Niño and warm pool El Niño. *J. Climate*, **22**, 1499–1515, https://doi.org/10.1175/2008JCLI2624.1.

——, J. Choi, S.-I. An, F.-F. Jin, and A. T. Wittenberg, 2010: Warm pool and cold tongue El Niño events as simulated by the GFDL CM2.1 coupled GCM. *J. Climate*, **23**, 1226–1239, https://doi.org/10.1175/2009JCLI3293.1.

Larkin, N. K., and D. E. Harrison, 2005: On the definition of El Niño and associated seasonal average U.S. weather anomalies. *Geophys. Res. Lett.*, **32**, L13705, https://doi.org/10.1029/2005GL022738.

Lian, T., D. Chen, Y. Tang, and Q. Wu, 2014: Effects of westerly wind bursts on El Niño: A new perspective. *Geophys. Res. Lett.*, **41**, 3522–3527, https://doi.org/10.1002/2014GL059989.

Manucharyan, G. E., and A. V. Fedorov, 2014: Robust ENSO across a wide range of climates. *J. Climate*, **27**, 5836–5850, https://doi.org/10.1175/JCLI-D-13-00759.1.

Neale, R. B., J. H. Richter, and M. Jochum, 2008: The impact of convection on ENSO: From a delayed oscillator to a series of events. *J. Climate*, **21**, 5904–5924, https://doi.org/10.1175/2008JCLI2244.1.

Newman, M., S.-I. Shin, and M. A. Alexander, 2011: Natural variation in ENSO flavors. *Geophys. Res. Lett.*, **38**, L14705, https://doi.org/10.1029/2011GL047658.

Okumura, Y. M., and C. Decer, 2010: Asymmetry in the duration of El Niño and La Niña. *J. Climate*, **23**, 5826–5843, https://doi.org/10.1175/2010JCLI3592.1.

Ren, H.-L., and F.-F. Jin, 2013: Recharge oscillator mechanisms in two types of ENSO. *J. Climate*, **26**, 6506–6523, https://doi.org/10.1175/JCLI-D-12-00601.1.

——, ——, M. F. Stuecker, and R. Xie, 2013: ENSO regime change since the late 1970s as manifested by two types of ENSO. *J. Meteor. Soc. Japan*, **91**, 835–842, https://doi.org/10.2151/jmsj.2013-608.

Reynolds, R. W., N. A. Rayner, T. M. Smith, D. C. Stokes, and W. Wang, 2002: An improved in situ and satellite SST analysis for climate. *J. Climate*, **15**, 1609–1625, https://doi.org/10.1175/1520-0442(2002)015<1609:AIISAS>2.0.CO;2.

Santoso, A., S. McGregor, F.-F. Jin, W. Cai, M. H. England, S.-I. An, M. McPhaden, and E. Guilyardi, 2013: Late-twentieth-century emergence of the El Niño propagation asymmetry and future projections. *Nature*, **504**, 126–130, https://doi.org/1038/nature12683.

Stevenson, S., 2012: Significant changes to ENSO strength and impacts in the twenty-first century: Results from CMIP5. *Geophys. Res. Lett.*, **39**, L17703, https://doi.org/10.1029/2012GL052759.

Taschetto, A. S., A. S. Gupta, N. C. Jourdain, A. Santoso, C. C. Ummenhofer, and M. H. England, 2014: Cold tongue and warm pool ENSO events in CMIP5: Mean state and future projections. *J. Climate*, **27**, 2861–2885, https://doi.org/10.1175/JCLI-D-13-00437.1.

Thompson, C., and D. Battisti, 2000: A linear stochastic dynamical model of ENSO. Part I: Model development. *J. Climate*, **13**, 2818–2832, https://doi.org/10.1175/1520-0442(2000)013<2818:ALSDMO>2.0.CO;2.

Vecchi, G. A., B. J. Soden, A. T. Wittenberg, I. M. Held, A. Leetmaa, and M. J. Harrison, 2006: Weakening of tropical Pacific atmospheric circulation due to anthropogenic forcing. *Nature*, **441**, 73–76, https://doi.org/10.1038/nature04744.

Wu, X., L. Deng, X. Song, G. Vettoretti, W. R. Peltier, and G. J. Zhang, 2007: Impact of a modified convective scheme on the Madden-Julian Oscillation and El Niño-Southern Oscillation in a coupled climate model. *Geophys. Res. Lett.*, **34**, L16823, https://doi.org/10.1029/2007GL030637.

Xiang, B., B. Wang, and T. Li, 2013: A new paradigm for the predominance of standing central Pacific warming after the late 1990s. *Climate Dyn.*, **41**, 327–340, https://doi.org/10.1007/s00382-012-1427-8.

Xie, R., F. Huang, F.-F. Jin, and J. Huang, 2015a: The impact of basic state on quasi-biennial periodicity of central Pacific ENSO over the past decade. *Theor. Appl. Climatol.*, **120**, 55–67, https://doi.org/10.1007/s00704-014-1150-y.

——, F.-F. Jin, and F. Huang, 2015b: An improved atmospheric component of Zebiak-Cane model for simulating ENSO winds. *J. Meteor. Soc. Japan*, **93**, 535–550, https://doi.org/10.2151/jmsj.2015-033.

Yeh, S.-W., J.-S. Kug, B. Dewitte, M.-H. Kwon, B. P. Kirtman, and F.-F. Jin, 2009: El Niño in a changing climate. *Nature*, **461**, 511–515, https://doi.org/10.1038/nature08316.

Zebiak, S. E., and M. A. Cane, 1987: A model El Niño–Southern Oscillation. *Mon. Wea. Rev.*, **115**, 2262–2278, https://doi.org/10.1175/1520-0493(1987)115<2262:AMENO>2.0.CO;2.